Engineering with Computers
https://doi.org/10.1007/s00366-025-02217-w

ORIGINAL ARTICLE

A hybrid Lattice-Boltzmann model for hydro-electrochemical modeling and sensitivity analysis of crystallization potential in nanoporous media. Part II: application to the identification and quantification of influencing factors of phosphate saturation

Fedor Bukreev[1,2] · Adrian Kummerländer[1,3] · Julius Jeßberger[1,3] · Dennis Teutscher[1,2] · Shota Ito[1,2] · Stephan Simonis[1,3] · Davide Dapelo[4] · Mohaddeseh M. Nezhad[4] · Hermann Nirschl[2] · Mathias J. Krause[1,2,3]

Received: 25 February 2025 / Accepted: 21 September 2025

Abstract
This paper series considers the process of hydro-electrochemical saturation in nano-scale porous media. In Part I, we introduced a novel, synchronous, and integrated numerical model for hydro-electro-chemo-dynamics simulation and sensitivity analysis of nanoscale crystallization potential, and validated each of its components separately. In this Part II, we apply this methodology to perform the integrated simulations of complex 2D and 3D nanopore systems that exhibit electrochemical, hydrodynamic, and crystallization phenomena, in pair with sensitivity analysis. The phenomenon chosen for this analysis is the formation of octa-calcium phosphate in the calcium silicate hydrate. A reactive Navier–Stokes–Poisson–Nernst–Planck equation system for three ions types in the moving fluid and in the presence of a dynamic electric field is discretized using lattice Boltzmann methods. Using automatic differentiation, simplified two-dimensional models of open and blind pores as well as a three-dimensional μCT scan of a porous rock are investigated with respect to the influences of electric surface potential, pore width and length, carrier fluid velocity and ion concentrations on octacalcium phosphate saturation. These simulations reveal new previously unknown insights into the crystallization process in nanopores—specifically, that narrow long blind pores with higher surface electric potential promote saturation probability. Moreover, large geometries with bigger pore systems accumulate more ions in their center locally in comparison to the smaller systems.

Keywords Nanoporous geometry · Phosphates crystallization · Saturation · Electro-chemistry · Lattice-Boltzmann method · Automatic differentiation

1 Introduction

The present Part II uses the integrated hydro-electro-chemo-dynamics sensitivity assessing solver we presented in Part I, to perform comprehensive simulations of the phosphate crystallization reaction—more specifically, to the octacalcium phosphate (OCP) saturation. This reaction is the main part of the P-RoC process, which is designed for phosphorus recovery from wastewater for re-utilisation in agriculture and the chemical industry [1]. The P-RoC process has a high potential for world economics and ecology protection due to its simplicity. An additional crystallization reactor installed in the sewage treatment plant would continuously produce calcium silicate hydrate (CSH) particles enriched with phosphates which can be used for further processing steps. In wastewater, an average concentration of phosphates is about

✉ Fedor Bukreev
fedor.bukreev@kit.edu

1 Lattice Boltzmann Research Group (LBRG), Karlsruhe Institute of Technology (KIT), Straße am Forum 8, 76131 Karlsruhe, Germany

2 Institute of Mechanical Process Engineering and Mechanics (MVM), Karlsruhe Institute of Technology (KIT), Straße am Forum 8, 76131 Karlsruhe, Germany

3 Institute for Applied and Numerical Mathematics (IANM), Karlsruhe Institute of Technology (KIT), Englerstraße 2, 76131 Karlsruhe, Germany

4 Department of Civil and Environmental Engineering, School of Engineering, University of Liverpool, Brownlow Hill, Liverpool L69 3GH, UK

Published online: 13 October 2025

13 M-% [2]. Unfortunately, state-of-the-art efficiency of the process is around 15–25 % [3], which is insufficient for industrial applications [4, 5]. Current macro-level modeling approaches face inherent limitations in further effectiveness improving of the process described above. Specifically, the existing framework based on adsorption isotherm ansatzes [6] employs empirically fitted functions to characterize reaction equilibrium [7], which restricts the conclusions that can be drawn about the underlying chemistry.

Apart from the crystallization kinetics itself, another important aspect is the transport of chemical species, which is by crystallization macro-modelling divided into diffusion from bulk to film around adsorbent micro-particles, film diffusion, surface and pore diffusion. They are described on a macro-level by distinct diffusivity coefficients that represent disparate behavior of transported species in the corresponding regions around and inside of the solid adsorbent. These coefficients are usually derived empirically and do not allow us to investigate the crystallization processes in detail. Conversely, nano-level simulation of the phosphate crystallization would allow to model the above-mentioned phenomena without empiricism. More in detail, the modellable phenomena are (cfr. Part I):

1. Migration of reacting ions from bulk to the pore entrance (diffusive, hydraulic and electric transport)
2. Migration of ions through pore volume (diffusive, hydraulic and electric transport)
3. Contact of ions with pore wall leading to dissolution of calcium cations
4. Saturation of reactants at the soil surface
5. Distinct nucleation of the adsorbate ion based crystal at the point with most appropriate conditions (saturation product above one and low surface tension)
6. Layer-wise growth of the crystal.

Nanoscale investigations of chemical processes have already been documented in the literature. Experimental and numerical (not CFD) studies demonstrated that the crystallization reaction of phosphate starts with the dissolution of calcium cations from the CSH pore surface [8, 9]. Concrete leaching (similar reaction to calcium dissolution in CSH) on multiple scales was simulated numerically by Su et al. [10]. Considering crystallization on the nanoscale, the incorporation of separate phosphate ions into the pore surface was modelled using the extended triple level method by Fukushi et al. [11]. The nucleation and crystallization basics are explained in [12]. Ionic reaction with nucleation and crystallization on microscale on the example of calcium carbonate crystal growth was experimentally investigated by Kim et al. [13].

In the context of computational fluid dynamics (CFD) and the Lattice-Boltzmann method (LBM), the general mineral precipitation in a porous domain with reactively changing porosity has been simulated by Ahkami et al. [14]. Due to the reaction mechanism, the saturation product plays the main role in the process. Despite this body of research, until now, the sensitivity of the saturation product with respect to design parameters, like pore size, carrier fluid velocity, Helmholtz potential, and reacting ion concentrations, on the pore level has not been analyzed.

This work specifically addresses this knowledge gap. In the first part, a hydro-electrochemical simulation system for nanoporous geometries was developed and validated against analytical solutions. Tests indicated that the internal Poisson calculation loop can be omitted for stationary or quasi-stationary scenarios, where changes in the Nernst–Planck and Navier–Stokes equations are much slower than changes in electric potential. The system's sensitivity analysis, using forward automatic differentiation (AD) and finite difference method (FDM), was validated. Accordingly, the model has demonstrated the ability to simulate surface ionic reactions at the nanoscale. In this work (Part II), we apply it to perform the integrated simulations of phosphate saturation, complemented by a sensitivity analysis to identify key influencing factors and pore behavior.

This work is structured as follows. First, 2D simulations of simplified models are performed (Sect. 3). A two-dimensional parameterized simplified simulation domain, which represents a resolved nanoporous system, is analyzed with the AD-based sensitivity assessment solver developed in Part I (Sect. 3.2). The following influence factors are investigated: surface electric potential, pore dimensions, bulk concentrations, and carrier fluid inlet velocity. Two geometries, respectively representing blind and open pores, are used (Sect. 3.3). Then, the same approach is applied to investigate a realistic three-dimensional porous system (Sect. 4). Special attention is paid to the electric surface potential, as it allows us to differentiate between pore types, and to the size of simulated geometry. The results of the 3D analysis are tested by varying the simulation setup parameters in Sect. 4.5. Finally, the main conclusions are summarized in

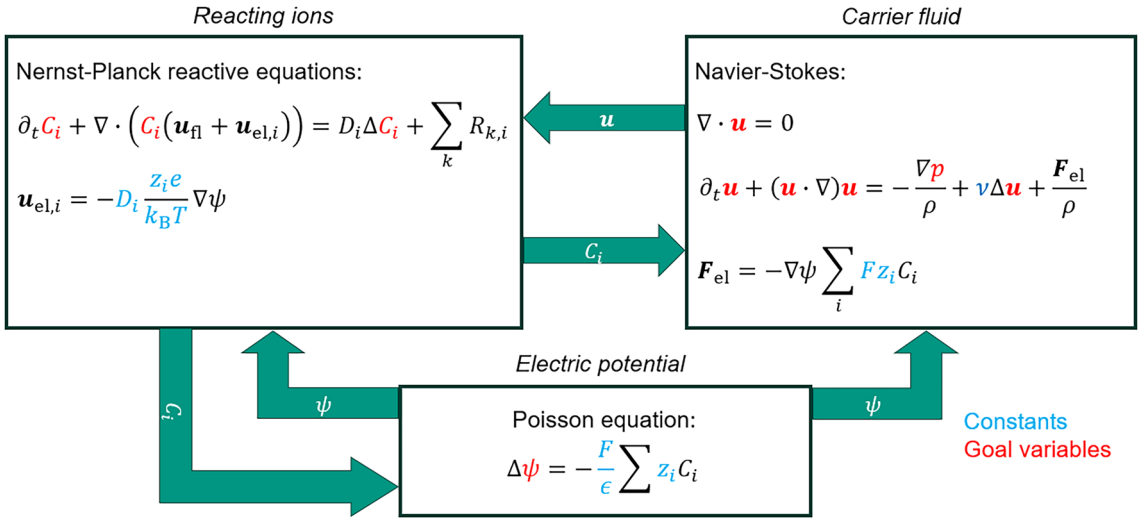

Fig. 1 Full Eulerian equation system for a hydro-electro-chemical simulation of an ionic supersaturation process and dissolution reactions in resolved nanopores (from Part I)

the Sect. 5. All the simulations are implemented using the *OpenLB* open-source software library [15]. The numerical runs that apply AD are parallelized using OpenMPI; all the others, via an MPI-based Multi-GPU approach [16].

2 Recap of the model

Within this work, we use the simulation model developed in Part I (cf. Fig. 1).

The model uses the Eulerian approach for all transported variables considering the fluid and ions as a continuum. The carrier fluid is described with electrically forced Navier–Stokes equations. The electrically laden calcium Ca^{2+} and hydrogen H^+ cations, as well as phosphate PO_4^{3-} anions, are modelled with three reactive Nernst–Planck equations. The electric field, which has a high impact on the considered nano-level, is calculated with the Poisson equation. The gained reactive Navier–Stokes–Poisson–Nernst–Planck equation (RNSPNPE) system is discretized using LBM for each system part. The built-up algorithm uses the Strang splitting assumption inside each global time step—variables computed in one equation are assumed to be constant by the computation of the further equations.

In the boundary cells around the solid surfaces, the dissolution reaction of calcium cations and saturation reactions of all considered ions happen in parallel.

$$CSH + 1.66H^+ \leftrightarrows 0.86Ca^{2+}, \tag{1}$$

$$8Ca^{2+} + 6PO_4^{3-} + 2H^+ \xrightarrow{\text{saturation}} Ca_8H_2(PO_4)_6 \downarrow . \tag{2}$$

The reaction rates *r* for both reactions can be expressed with the same formula

$$r = \frac{k_{sr}}{\triangle x}(\Omega - 1)^n, \tag{3}$$

$$\Omega = \left({}^{IAP}/_{K_{sp}} \right)^{1/\sigma_T}, \tag{4}$$

where k_{sr} is the surface-specific reaction rate constant, Ω—saturation product of the species, *n*—reaction order, *IAP*—ionic activity product, K_{sp}—saturation point constant and σ_T—Temkin coefficient.

The simulation algorithm can be summarized as:

// Initialization
if boundary cell **then**
  Apply ADE boundary conditions with initial values for PE
  for each solved ion **do**
    Apply ADE boundary conditions with initial values for RNPE
  end for
  Apply boundary conditions with initial values for NSE
end if
Initialize f_j^{eq} with given initial values
// Main simulation loop
for each $t \leq t_{\max}$ **do**
  // LB simulation steps
  while $\frac{\frac{1}{N_t}\sum_l^{N_t}(\psi_{\mathrm{avg},l}-\sum_m^{N_t}\psi_{\mathrm{avg},m})^2}{\sum_m^{N_t}\psi_{\mathrm{avg},m}} > \varepsilon$ **do** *// Poisson loop*
    Collision and streaming for PE of a vector $(f_{j,\mathbf{PE}}, \partial_\alpha f_{j,\mathbf{PE}})$
  end while
  for each solved ion **do**
    if boundary cell **then**
      Apply ADE boundary conditions for RNPE
    end if
    Collision and streaming for RNPE of a vector $(f_{j,i,\mathrm{RNPE}}, \partial_\alpha f_{j,i,\mathrm{RNPE}})$
  end for
  if boundary cell **then**
    Apply boundary conditions for NSE
  end if
  Collision and streaming for carrier fluid NSE of a vector $(f_{j,\mathrm{NSE}}, \partial_\alpha f_{j,\mathrm{NSE}})$
  // Post-processing
  Calculate Poisson eq. source term S_{PE} and $\partial_\alpha S_{\mathrm{PE}}$
  for each solved ion **do**
    Calculate $\boldsymbol{u}_{\mathrm{el}}$ for each solved ion and their derivatives w.r.t. α
  end for
  Calculate $\boldsymbol{F}_{\mathrm{el}}$ for the carrier fluid and its derivative w.r.t α
  for each boundary cell **do**
    Calculate r_{diss}, $\partial_\alpha r_{\mathrm{diss}}$
    Calculate $\Omega_{\mathrm{OCP}} = \left(\frac{\mathrm{IAP}_{\mathrm{OCP}}}{K_{\mathrm{sp,OCP}}}\right)^{\frac{1}{\sigma_{\mathrm{T,OCP}}}}$ and $\partial_\alpha \Omega_{\mathrm{OCP}}$
  end for
end for

Due to the existing steady state in the regarded application, only one Poisson equation calculation step per global time step is performed. The chosen discretization, including boundary treatments, exhibits first-order convergence, as demonstrated through validation tests in Part I on individual system components and their combination against existing analytical solutions. Forward AD for sensitivity computation is coupled to the LBM solver, whereby each calculated variable is extended to a vector, whose further components are derivatives of this variable with respect to the chosen operational parameters.

Each micro-particle has contact with the bulk on both outer and inner surfaces, necessitating the consideration of both in our research. According to IUPAC [17], the inner surfaces or inter-particle pores can be categorized into closed, blind, and open pores, each with distinct geometrical shapes. Closed pores, being inaccessible to dissolved ions from outside, are excluded from the simulations. We will investigate the open and the blind pores separately, focusing on the following parameters: surface Helmholtz potential, pore dimensions, ion concentrations, and carrier fluid inlet velocity.

3 2D simulations

In this section, we resolve the geometry of single particles–each featuring either open or blind pores–in a simplified 2D setup.

3.1 Simulation setup and boundary conditions for 2D pore geometries

In the current research, ion accumulation at nano-scale on solid walls in porous micro-systems is investigated. For the two-dimensional investigations, two square domains are chosen (Fig. 2). The geometry (a) represents an open pore test case, whereby the option (b) is designed for blind pores investigation. The two options are simulated with coupled sensitivity analysis, starting by nanopores diameter of 42.8 nm. The distance between the outer solid bodies and the domain boundaries is set to 12 Debye lengths (one Debye length being the distance at which the electric potential ψ falls by $\frac{1}{e}$) computed for 0.1 $\mathrm{mol\,m^{-3}}$ of phosphate anion. Such distance is chosen in order to make sure that the electric potential at the domain boundaries remains negligible. At the small simulation scales, the cell size has influence on the physical computation model. At higher Knudsen numbers:

$$Kn = \frac{M}{\rho N_A \pi d_m^2 \triangle x} \tag{5}$$

[18], the additional Knudsen diffusion and some other effects should be considered, which would complicate the existing model much more and are not included in the current research. Here, d_m is the molecule diameter, and M is the molar mass of water, which is the specie with the highest concentration. Water is also the carrier fluid and has the largest mean free path among all considered components (Table 1) in the solution, and its concentration is incomparably higher than the other ones. The cell size $\triangle x$ is set to $0.09 \cdot Kn$. The solid body corner length is set to 60 cells.

The domain boundaries **A**, **B**, **C**, and **D** are treated identically, with the electric potential set to zero. The carrier fluid is assigned a constant flow velocity in the positive x-direction (**A**, **B**, **C**, **D**), and these outer boundaries are handled uniformly to avoid any influence from differing boundary conditions and to prevent instabilities. Hydrogen and phosphate ions are each given fixed concentrations of 0.3 and 0.1 $\mathrm{mol\,m^{-3}}$, respectively, while their concentrations inside the domain are initialized to zero to capture the diffusion of ions from the bulk to the pore openings and into the pores. The concentration of calcium cations, on the other hand, is set to zero at the boundaries to avoid undesirable backflow of these ions and improve boundary stability.

At the Helmholtz layer next to the solid surface (boundary **E**), the electric potential is set to a constant value of ± 0.01 V. Its impact is investigated in the current work as well. The transported ions are reflected at the solid walls, whereby in the bulk cells touching the boundaries, their concentration can be changed according to the corresponding reaction term $\sum_k R_{k,i}$. In LBM this corresponds to the

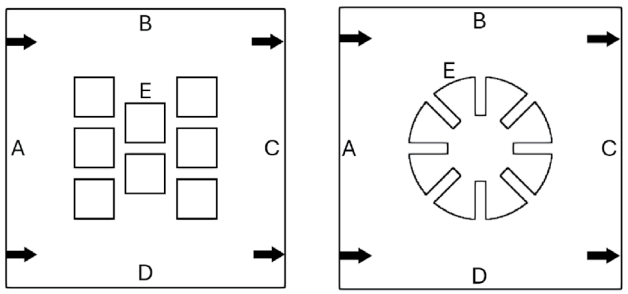

(a) Open pores (b) Blind pores

Fig. 2 Simulation domains. Open pores—42.8 nm wide, 84 nm length-per-block. Blind pores—42.8 nm wide, 123.5 nm deep

Table 1 Simulation parameters and constants

Parameter	Value
Dielectric constant ϵ [$\mathrm{CV^{-1}m^{-1}}$]	$6.95 \cdot 10^{-10}$ [20]
Faraday constant F [$\mathrm{Cmol^{-1}}$]	96485.33
Boltzmann constant k_B [$\mathrm{VCK^{-1}}$]	$1.38065 \cdot 10^{-23}$
Elementary charge e [C]	$1.602177 \cdot 10^{-19}$
Surface potential ψ_0 [V]	-0.01
Inlet velocity u_i [$\mathrm{ms^{-1}}$]	0.2
Fluid viscosity ν [$\mathrm{m^2\,s^{-1}}$]	10^{-6} [20]
Water mean free path λ_{H2O} [m]	$1.26 \cdot 10^{-10}$ [18]
Avogadro number N_A [$\mathrm{mol^{-1}}$]	$6.02 \cdot 10^{23}$
Hydrogen ion diffusion constant D_{H^+} [$\mathrm{m^2\,s^{-1}}$]	$9.31 \cdot 10^{-9}$ [21]
Phosphate ion diffusion constant $D_{PO_4^{3-}}$ [$\mathrm{m^2\,s^{-1}}$]	$0.612 \cdot 10^{-9}$ [21]
Calcium ion diffusion constant $D_{Ca^{2+}}$ [$\mathrm{m^2\,s^{-1}}$]	$0.792 \cdot 10^{-9}$ [21]
OCP saturation constant $K_{sp,OCP}$ [$(\mathrm{mol\,m^{-3}})^{16}$]	$10^{-48.86}$ [22]
OCP Temkin coefficient $\sigma_{T,OCP}$	1 [9]
CSH dissolution rate coefficient k_{CSH} [$\mathrm{mol\,m^{-2}\,s^{-1}}$]	$3.1 \cdot 10^{-11}$ [9]
CSH saturation constant $K_{sp,CSH}$ [$(\mathrm{mol\,m^{-3}})^x$]	$10^{11.15}$ [9]
CSH Temkin coefficient $\sigma_{T,CSH}$	16 [23]
Phosphor acid concentration $C_{H_3PO_4}$ [$(\mathrm{mol\,m^{-3}}$]	0.1
Temperature T [K]	298.15
Debye–Hückel coefficient A [$\sqrt{(\mathrm{m^3\,mol^{-1}})}$]	0.016102
Debye–Hückel coefficient B [$\sqrt{(\mathrm{m^3\,m^{-2}\,mol^{-1}})}$]	$1.0391 \cdot 10^8$
Molecular distance Ca-w [m]	$2.33 \cdot 10^{-10}$ [24]
Knudsen number Kn	0.09
Discretization parameters	
Cell size $\triangle x$ [m]	$1.40045 \cdot 10^{-9}$
Time step Poisson lattice $\triangle t_{PE}$ [s]	$2.45159 \cdot 10^{-19}$
Time step momentum lattice $\triangle t_{NSE}$ [s]	$2.61503 \cdot 10^{-13}$
Time step ions lattice $\triangle t_{NPE}$ [s]	$4.80703 \cdot 10^{-11}$

bounce-back boundary condition together with a source term applied in the boundary cells. At the Knudsen number of 0.09, which is here the case, the free-slip regime for the carrier fluid velocity is considered [19]. It is a simplification of reality, but this Knudsen number value belongs to the upper border of the slip regime, where we assume a slip factor striving to zero–zero-gradient velocity boundary or free-slip. The electric velocity, whose influence is much higher than the influence of the carrier fluid velocity, is still considered at the boundary cells. Knudsen diffusion and confinement effects near the wall are not considered in terms of this work. Knudsen diffusion is still much smaller than the Fickian one in the slip regime.

The list of the setup parameters and constants is shown in Table 1.

3.2 Investigation of saturation on the 2D porous object

Given the significant uncertainty surrounding the Helmholtz electric potential at solid surfaces, we consider two scenarios, with potentials being set at −0.01 and +0.01 V. We then investigate the sensitivities of the corresponding parameters. The variables for which derivatives are calculated include carrier fluid inlet velocity, pore width, initial concentrations of hydrogen and phosphate ions, and electric potential at the block's solid surface (boundary **E**).

The primary evaluation criterion for crystal formation is the saturation product Ω. If it is larger than one, nucleation and crystallization on the surface are enabled. Of particular interest is the temporal development of the spatially averaged and maximal saturation products, along with their partial derivatives. The spatially averaged values are computed as follows:

$$\Omega_{L^1}(t) = \frac{1}{N_{\text{node}}} \sum_{x_i=1,\Omega(x_i)>0}^{N_{\text{node}}} \Omega(x_i,t), \tag{6}$$

$$(\partial_\phi \Omega)_{L^1}(t) = \frac{1}{N_{\text{node}}} \sum_{x_i=1,\Omega(x_i)>0}^{N_{\text{node}}} \partial_\phi \Omega(x_i,t), \tag{7}$$

where ϕ represents the variable with respect to which the derivative is taken.

Figures 3 and 4 illustrate the saturation products and their sensitivities for different Helmholtz potentials across geometries (a) and (b). The left column presents the spatially averaged values, while the right column shows the behavior of the maximal values.

3.2.1 Saturation product development

Averaged and maximal saturation product development are shown in Fig. 3a, b. The development of the saturation product varies significantly between geometries (a) and (b). Despite their shallower depth (for the same width), blind pores exhibit significantly higher saturation levels, which do not reach equilibrium within the investigated time frame. Conversely, in the case of open pores, the Helmholtz surface potential has no significant impact on the saturation product value. However, in blind pores with a positive potential, the saturation of OCP is significantly enhanced.

Figure 5 displays the spatial distribution of the saturation product at time t=20 µs. It is evident that saturation within the pores is much higher than on the outer particle surface. The maximal values of the saturation product are located closer to the center of the geometry in the case of open pores and at the ends of blind pores. Consequently, further investigation focuses on the behavior of saturation within the pores.

To conclude, saturation within the pores is significantly higher for both Helmholtz potentials compared to the outer particle surfaces; especially high it is in the blind pore dead ends.

3.2.2 Helmholtz potential influence

Figure 3c, d show the influence of the surface electric potential of solid blocks on the saturation product development. For open pores, the sensitivities indicate that to increase the average saturation product, the Helmholtz surface potential should be set closer to zero. However, the maximal saturation value is achieved at a slightly negative potential (cfr. Fig. 3b). In contrast, for blind pores, a different behavior is observed. To maximize the average saturation product, the potential should be slightly positive, as can be observed in further simulations with 0.02 V and 0.2 V as surface potential values. Moreover, increasing the positive potential value at the point of maximum saturation within the pore enhances the probability of oversaturation.

In synthesis, a positive Helmholtz surface potential enhances saturation at the point inside a pore where the saturation product reaches its maximum.

3.2.3 Hydrogen cations concentration influence

The averaged and maximal sensitivities with respect to hydrogen ion concentration are shown in Fig. 3e, f. In open pores, ion accumulation increases with rising hydrogen concentration for both negative and positive surface potentials. However, a positive potential leads to a higher derivative with respect to the hydrogen ion concentration.

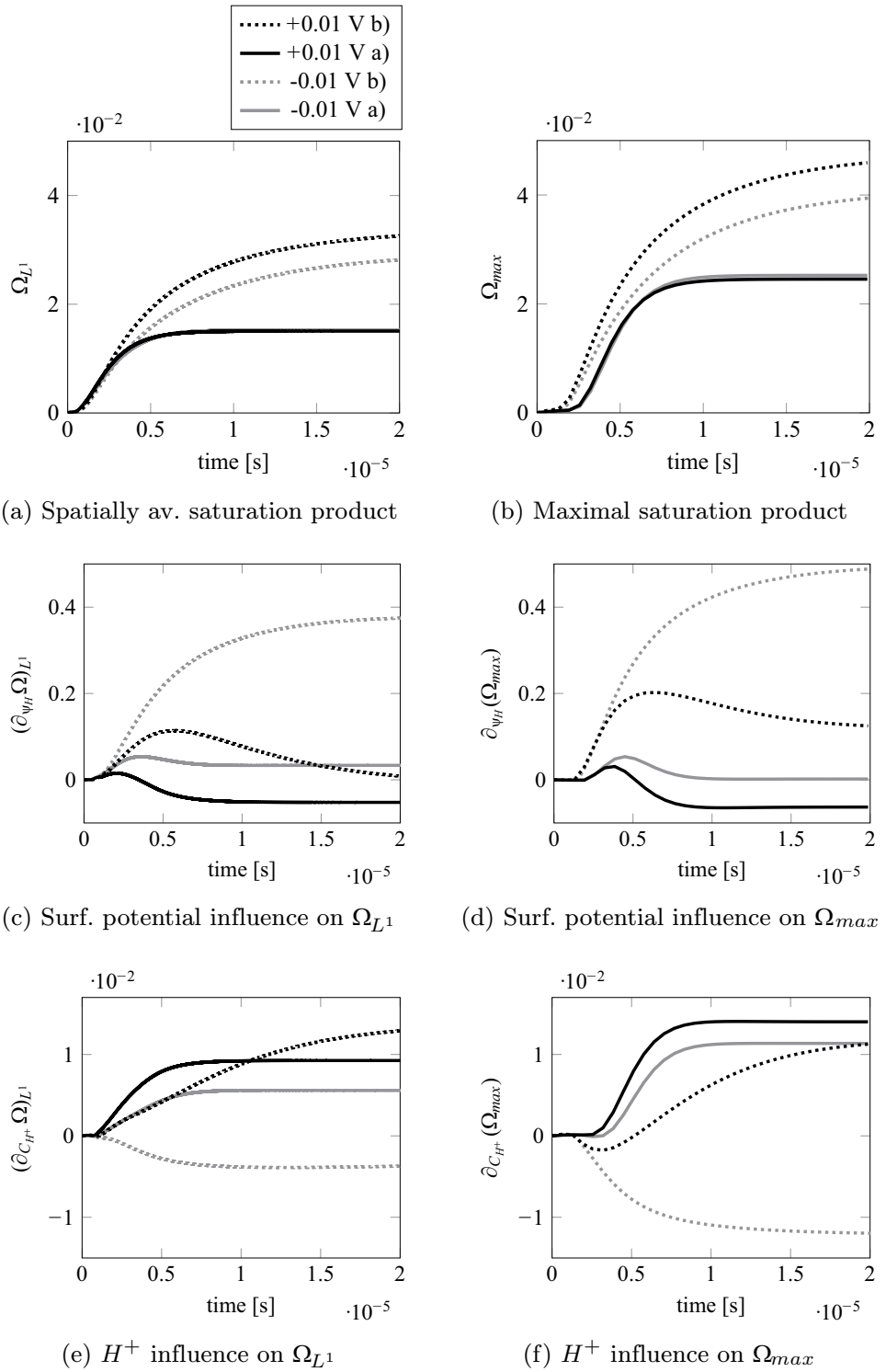

(a) Spatially av. saturation product

(b) Maximal saturation product

(c) Surf. potential influence on Ω_{L^1}

(d) Surf. potential influence on Ω_{max}

(e) H^+ influence on Ω_{L^1}

(f) H^+ influence on Ω_{max}

Fig. 3 Maximal and spatially averaged developments of saturation product Ω and its derivatives with respect to surface potential ψ_H, hydrogen and phosphate concentrations H^+, PO_4^{3-}, pore width and inlet carrier fluid velocity u_{inlet} on the a) and b) geometries by opposite Helmholtz potentials of ± 0.01 V. Part I/II

This phenomenon can be explained by the fact that cations are repelled from the surface, which is counterbalanced by diffusive transport. Higher concentrations enhance the diffusive transport of ions. In blind pores with a positive surface potential, the sensitivity to hydrogen concentration is consistently positive. Conversely, with a negative potential, the sensitivity is always negative, indicating that hydrogen is attracted to the surface by the electric force, and this force is sufficient to achieve OCP oversaturation even at lower concentrations.

Thus, because a positive surface potential is preferable based on the observations in the previous section, we

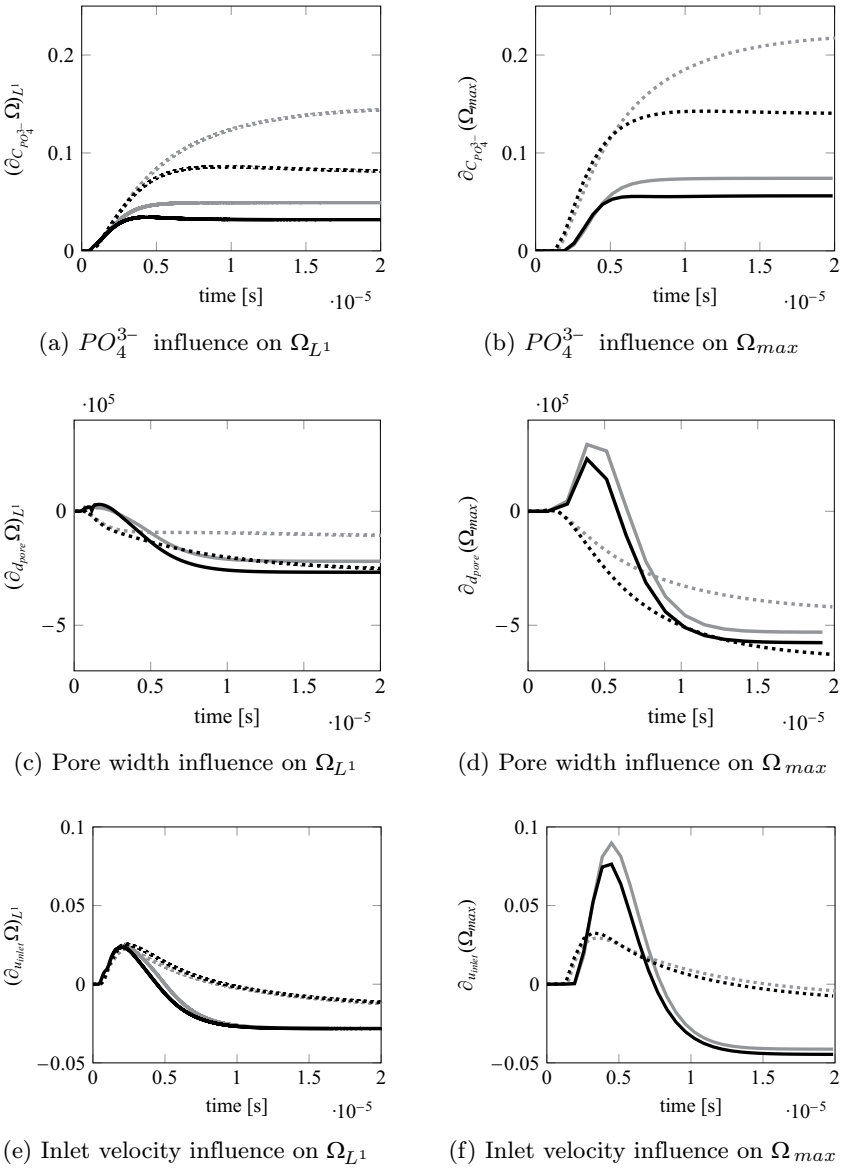

(a) PO_4^{3-} influence on Ω_{L^1}

(b) PO_4^{3-} influence on Ω_{max}

(c) Pore width influence on Ω_{L^1}

(d) Pore width influence on Ω_{max}

(e) Inlet velocity influence on Ω_{L^1}

(f) Inlet velocity influence on Ω_{max}

Fig. 4 Maximal and spatially averaged developments of saturation product Ω and its derivatives with respect to surface potential ψ_H, hydrogen and phosphate concentrations H^+, PO_4^{3-}, pore width and inlet carrier fluid velocity u_{inlet} on the a) and b) geometries by opposite Helmholtz potentials of ± 0.01 V. Part II/II

recommend increasing hydrogen concentration whenever feasible.

3.2.4 Phosphate anions concentration influence

Figure 4a, b illustrate the impact of phosphate anions concentration. In all cases, an increase in phosphate concentration consistently promotes a rise in the saturation product. As illustrated above, the sign of the surface potential influences the sensitivity. For anions, diffusive transport must overcome the resistance of electric force in the case of a negative Helmholtz potential, resulting in higher sensitivity.

As such, we recommend increasing the phosphate concentration whenever feasible, irrespective of the value of the surface potential.

3.2.5 Pore dimensions influence

The pore dimensions deliver the highest impact on the saturation product. In the 2D case, the parameters considered for sensitivity analysis are pore width and length.

Pore width: Figure 4c, d illustrate the influence of pore width over the saturation product. In all the considered scenarios, pore width consistently shows negative sensitivity towards the end of the simulation. Initially, the derivative curves increase until the maximum possible volume filling of hydrogen and phosphate ions is achieved. The maxima are significantly smaller for blind pores compared to open ones due to geometric differences. In geometry (a), the total length of open pores is greater than the combined length of the blind ones, requiring more time to fill the open pores with ions from the bulk. This time can be determined from

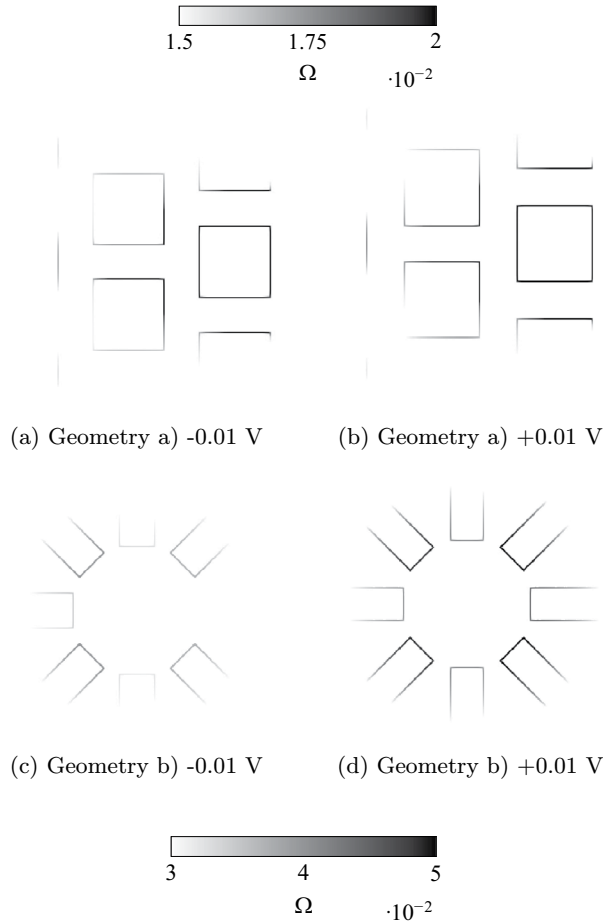

Fig. 5 Saturation product spatial distribution by geometries a) and b) by negative and positive Helmholtz potentials at the simulation final (20 µs)

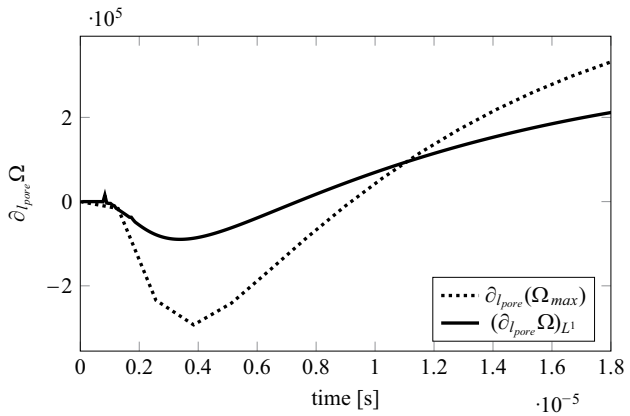

Fig. 6 Development of the average and maximal saturation product sensitivity with respect to pore depth by geometry b) and positive Helmholtz potential

the plot by reading the time where the curves cut the x-axis. After reaching the sensitivity maxima, the curves decline to relatively constant negative values because narrow pores restrict the outflow of dissolved calcium cations.

Therefore, we recommend minimizing pore width. Although this slows ion transport from the bulk, it leads to a higher saturation product.

Pore length: Figure 6 shows the saturation product derivative with respect to pore length, calculated for geometry (b) with a positive Helmholtz potential, as this setup yields the highest saturation among those tested. Initially, while the pores have not yet reached the maximum possible concentration of incoming ions, the derivative is negative. After this point, the derivative starts to increase and becomes positive, resulting in a higher maximum achieved saturation product.

Concluding, pores should be deeper to accumulate more reacting ions inside them.

3.2.6 Influence of the inlet velocity

The sensitivity analysis with respect to inlet velocity is shown in Fig. 4e, f. Depending on the pore type and its specific arrangement within the geometry, the carrier fluid velocity can influence saturation behavior in various ways.

Open pores: The impact of carrier fluid inlet velocity is more pronounced in open pores compared to blind pores. An analysis of the maximum of the derivative graph provides insight into the time required to fill the pore volume with reacting ions, similarly to the case of the influence of pore size. The carrier fluid, moving at a velocity determined by the choice of the boundary conditions, reduces the accumulation of dissolved calcium ions in the boundary cells from a certain moment onward. At the beginning, the carrier fluid fills the pore volume with ions, which is why the sensitivity is positive, but after that it sweeps the ions away and hinders the rise of saturation product. This negative effect is more pronounced in open pores, where the fluid can pass through the entire geometry with less resistance. Figure 7 illustrates the distribution of calcium cations in open pores for setups with 0.2 ms^{-1} inlet velocity and without.

It is clear that the absence of the carrier fluid movement promotes accumulation of the ions and an increasing of the saturation product.

Blind pores: For the blind pores (geometry b), we compare the sensitivities and saturation products among the pore-end centers on the right, upper, left, and bottom sides, as illustrated in Fig. 8.

A dead zone forms leeward of the geometry, allowing phosphate ions to accumulate and leading to the highest saturation product at point C. Towards the end of the simulation, all derivatives with respect to the velocity tend towards negative values or zero. At point C, the influence of surface potential also turns negative, unlike in other pores. The reduction of the size of the dead zone in geometries with deeper and narrower pores can be attributed to spatial

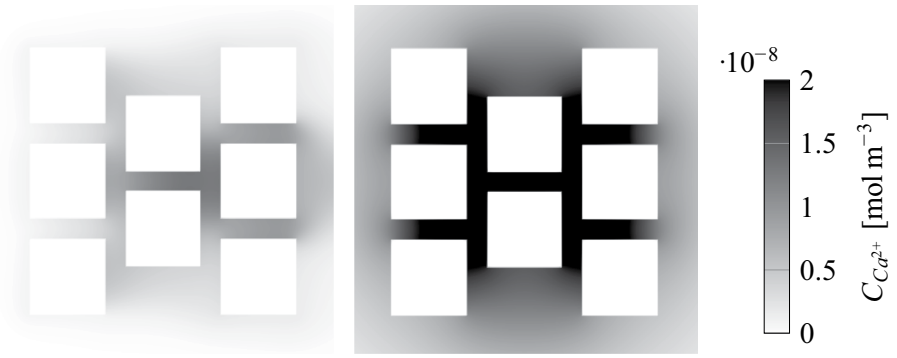

(a) With inlet velocity (b) W/o inlet velocity

Fig. 7 Accumulation of the calcium cation concentration at 13.46 µs with 0.2 ms^{-1} carrier fluid inlet velocity and without

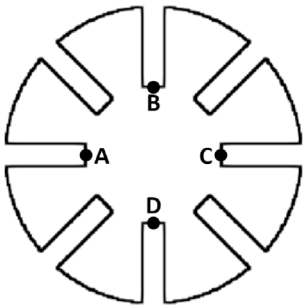

(a) Measurement points

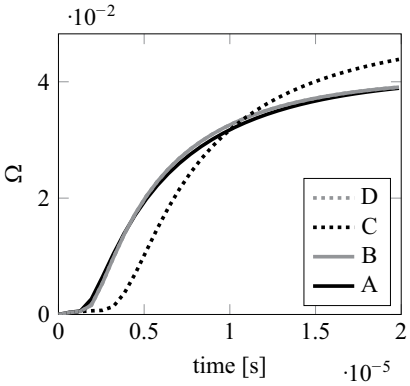

(b) Saturation product

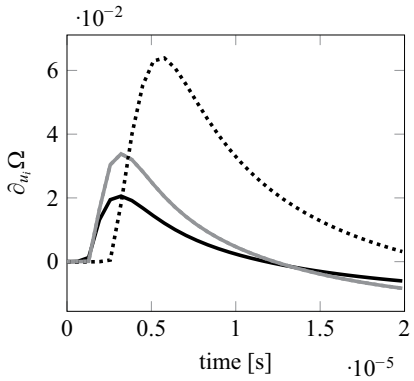

(c) Sensitivity with respect to velocity

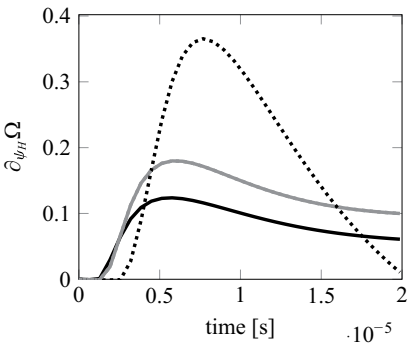

(d) Sensitivity with respect to Helmholtz potential

Fig. 8 Velocity influence on the saturation product and its sensitivities at the ends of blind pores by geometry b)

interactions among ions in the dead zone. Calcium and hydrogen ions are compelled to exit the pore, leading to a lower saturation product at point C. The development of the saturation product and spatial ion distribution at the end of the simulation is depicted in Fig. 9.

In the current OCP stoichiometric formula, calcium cations exert the largest influence on the saturation product (Fig. 9a, b). The calcium spatial distribution plays the largest part in determining the spatial distribution of the saturation product despite its very low concentration compared to hydrogen and phosphate; indeed, the cell with maximal calcium concentration is at the same time the cell with the highest saturation product. Therefore, to achieve oversaturation, conditions should be optimized for maximal accumulation of calcium in the pores.

It can be deduced that a high inlet carrier fluid velocity accelerates the filling of pores with reactants, but at the same time reduces the overall saturation product in the entire domain for open pores. In blind pores, the carrier fluid can redistribute ions such that saturation may increase in shallower pores while decreasing in others.

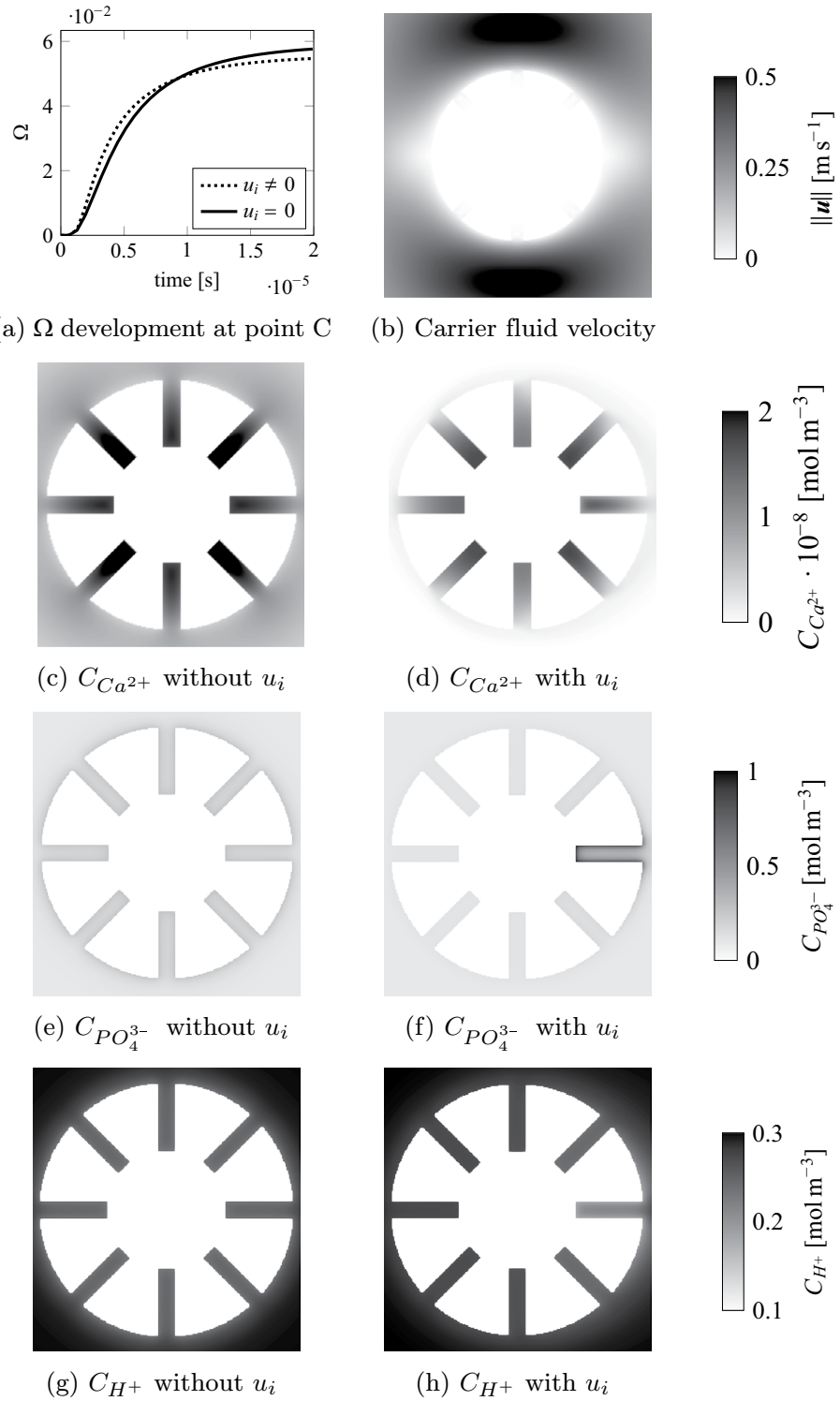

(a) Ω development at point C (b) Carrier fluid velocity

(c) $C_{Ca^{2+}}$ without u_i (d) $C_{Ca^{2+}}$ with u_i

(e) $C_{PO_4^{3-}}$ without u_i (f) $C_{PO_4^{3-}}$ with u_i

(g) C_{H^+} without u_i (h) C_{H^+} with u_i

Fig. 9 Comparison of the saturation product behavior and ions concentrations at the calculation end by simulations with and without carrier fluid velocity. Velocity direction is from left to right

3.3 Validation of 2D analysis results on modified geometries

In order to test the generality of the observations traced above, two parametrized simulations—with one open (a) and one blind pore (b)—are performed (Fig. 10). The parameters are varied according to the sensitivities in Table 2.

The temporal development of average and maximal saturation products is shown in the Fig. 11.

The modified boundary parameters and pore shapes in the modified 2D geometries lead to a much higher saturation.

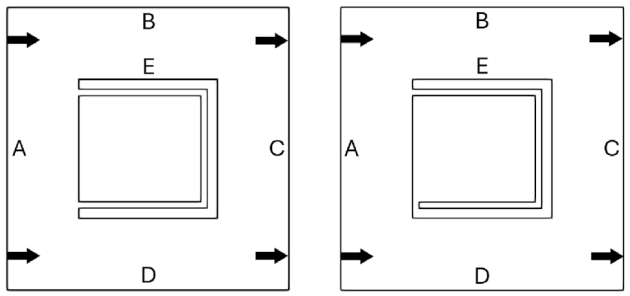

(a) Open pores - II (b) Blind pores - II

Fig. 10 Simulation domains

Table 2 Parameter optimization

Setup	I	II
d_{pore} [nm]	42.8	10.7
ψ_H [V]	+0.01	+0.01
$C(H^+)$ [(mol m^{-3}]	0.3	6
$C(PO_4^{3-})$ [(mol m^{-3}]	0.1	1
u_i [ms^{-1}]	0.2	0

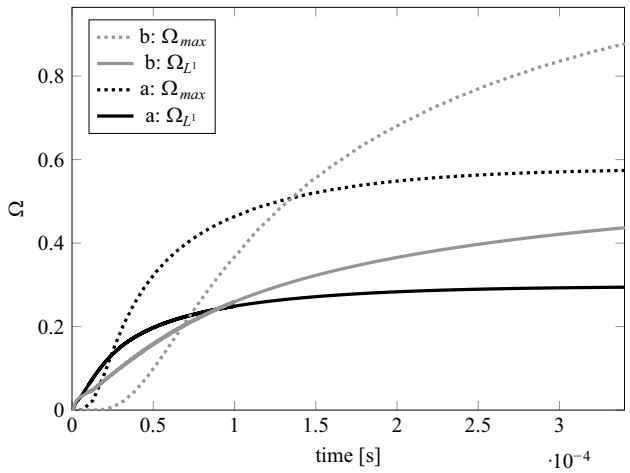

Fig. 11 Average and maximal saturation product development by modified pore geometries (a—open pore, b—blind pore)

The maximal saturation product observed in the blind pore surpasses the value of 1 after 550 µs and induces nucleation and crystallization in that lattice cell. The saturation in the open pore reaches a steady state twice as fast as in the blind-pore case due to the presence of two inlets that allow hydrogen and phosphate to diffuse in while calcium ions diffuse out.

Figure 12 depicts the saturation product and ion concentrations distributions at the end of simulation. In the open pore, the maximum saturation product is observed at the center, equidistant from both ends. In contrast, in the blind pore, the maximum occurs at the blind end. To understand these distributions, the individual ion concentrations must be considered. By the end of the simulation, the hydrogen cation concentration is uniformly distributed throughout the computational domain due to its relatively high diffusion coefficient, which overcomes the influence of the electric force. In contrast, phosphate anions are attracted to the solid surface, resulting in higher concentrations at the boundary cells compared to the bulk. The main difference between the two considered geometries lies in the distribution of calcium ion concentration. In an open pore, calcium ions flow out and accumulate only at the pore center, where the total transport velocity $\boldsymbol{u}_{t,i} = \boldsymbol{u}_{fl} + \boldsymbol{u}_{el,i} - D_i \frac{\nabla C_i}{C_i}$ approaches zero. In a blind pore, the transport path is approximately twice as long, and the calcium velocity remains low over a greater distance. Since the outlet direction is singular, the calcium removal rate is halved, allowing for more efficient ion accumulation. The total velocity at the end of the simulation is visualized in Fig. 13.

The step-wise parameter optimization of geometries a) and b) is provided in the supplementary materials. The applied changes lead to oversaturation in the blind pore and onset of crystallization, confirming the conclusions of the sensitivity analysis.

It can also be stated that there is a minimal surface-area-to-volume ratio (in 2D, perimeter-to-area) needed in order to reach an oversaturated solution state after which precipitation or crystallization can occur. Also, oversaturation probability grows with this ratio. Increasing the Helmholtz potential can increase this ratio to some degree. Considering the phosphate binding to CSH, the probability of achieving oversaturation and following crystallization grows with the pH factor. In contrast, an increase in the carrier fluid velocity hinders the accumulation of calcium cations at the boundary cells above a certain threshold, and for this reason, increasing this value is not advisable.

4 Investigation of saturation on a realistic 3D geometry

To investigate the saturation behavior of a real porous micro-system, a three-dimensional setup is employed using a scaled pore-level CT scan of an Estaillades carbonate microstructure [25]. This setup maintains the same cell size and Knudsen number as the 2D simulation. A quarter of the microstructure file ($\alpha = \frac{V_{sim}}{V_{\mu CT}} = 25\%$), with a length of 180 nanometers and resolved with 114 cells, is surrounded by 50 pure fluid cells on each side. The same boundary conditions as the previous 2D setup are applied. The new boundary planes which have not existed in the 2D case are treated in the same way as the boundaries A, B, C, D. The

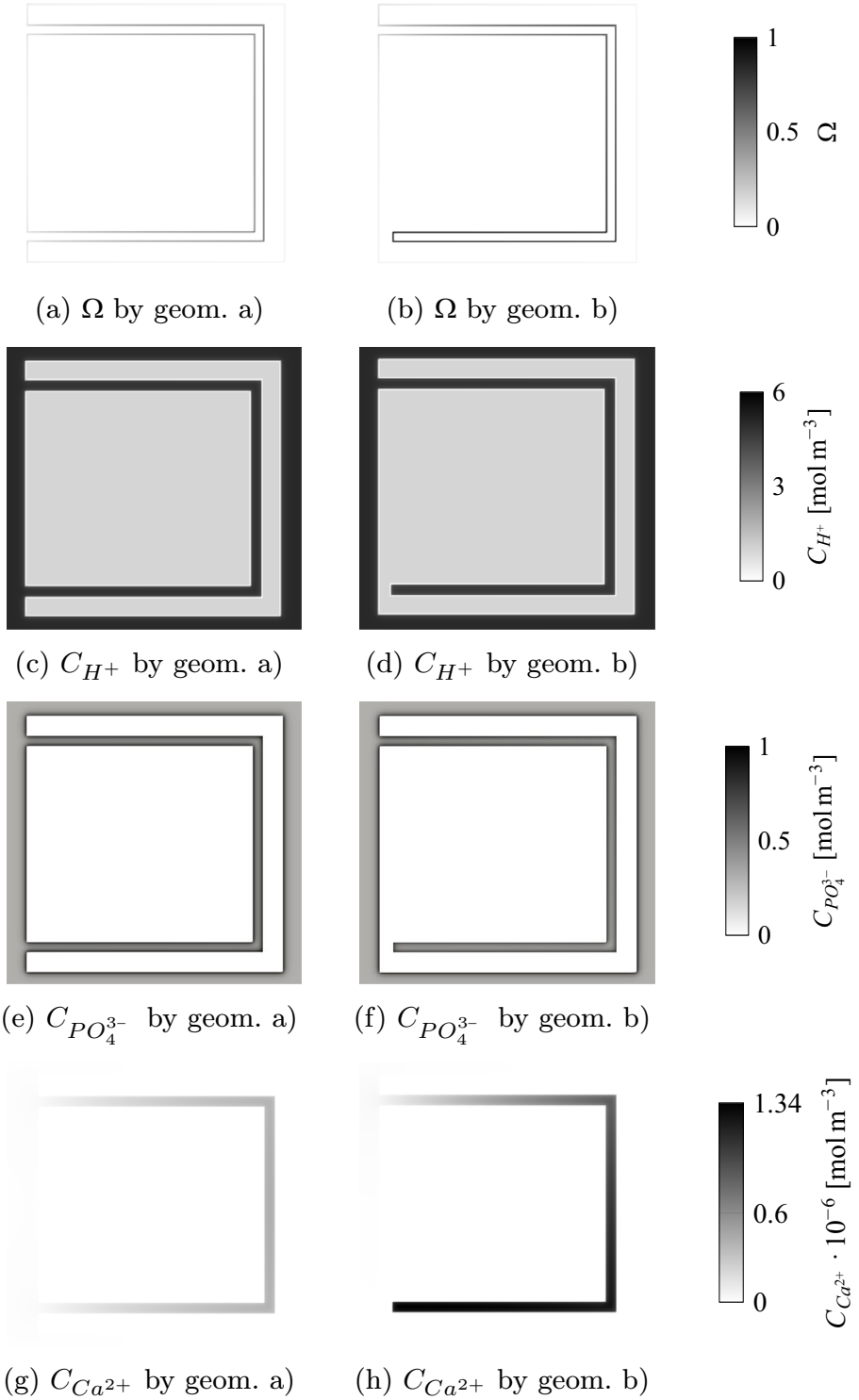

Fig. 12 Spatial distribution of saturation product Ω and ion concentrations H^+, PO_4^{3-}, Ca^{2+} by geometries a) and b) at simulation final (345 μs)

geometry and pore size distribution of the system are shown in Fig. 14.

To investigate the effects of surface Helmholtz potential, ion concentrations, and carrier fluid inlet velocity on crystallization within the nanoporous microstructure, we analyze the temporal evolution of both maximal and spatially averaged saturation product sensitivities. Additionally, we examine the instantaneous spatial distributions of these sensitivities, as shown in Figs. 15 and 16.

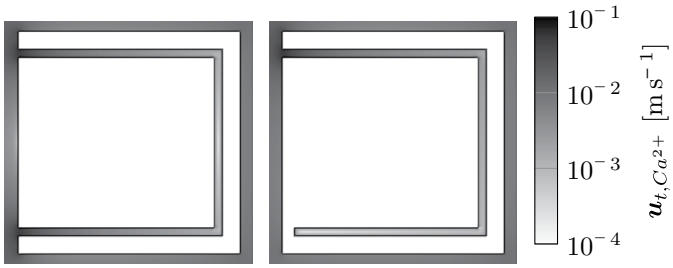

(a) Open pore a) (b) Blind pore b)

Fig. 13 Calcium cation total velocity distribution ($\boldsymbol{u}_{t,i} = \boldsymbol{u}_{fl} + \boldsymbol{u}_{el,i} - D_i \frac{\nabla C_i}{C_i}$) at the simulation final (345 µs)

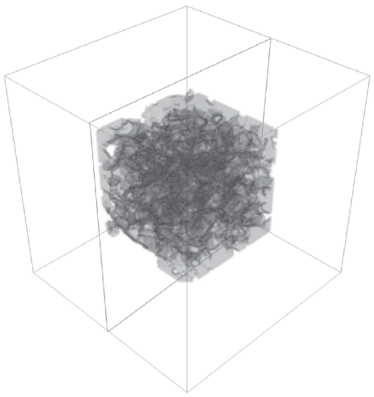

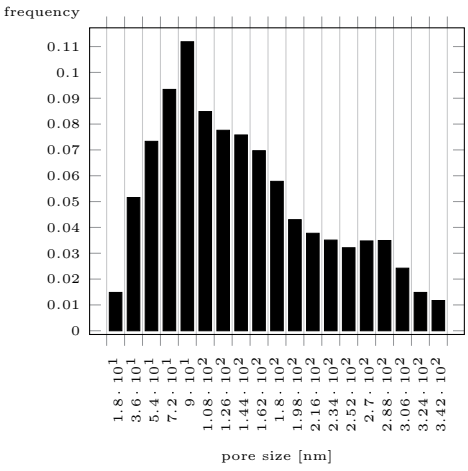

(a) 3D setup geometry (b) Pore size distribution

Fig. 14 3D geometry with porous body and its pore size distribution [25]. The blue lines show the cut plane used for the further evaluation

4.1 Helmholtz potential influence

The sensitivity with respect to surface electric potential (Fig. 15d, e) distinguishes between different types of pores in the realistic geometry. Pores exhibiting a negative derivative are identified as open pores, while those with a positive sensitivity are classified as blind pores, which also exhibit the highest saturation product. Given that the average sensitivity is negative, most pores are of the open type, explaining the significant difference between average and maximal saturation products. This sensitivity also has the highest norm among others, indicating that an increase in potential can lead to stronger saturation.

We can conclude that using sensitivity analysis with respect to surface potential in a realistic geometry allows for categorizing pores according to their types.

4.2 Influence of the inlet velocity

The impact of the inlet velocity is presented in Fig. 15g, h. The average derivative of the saturation product with respect to carrier fluid inlet velocity remains negative, similarly to what was observed in the 2D simulations, given that most pores in the current geometry are open. However, the derivative in cells with maximal saturation product is positive, indicating a contrasting effect. An examination of the spatial distribution of this sensitivity reveals that in pores with high saturation, the derivative tends to be positive. This phenomenon can be attributed to phosphate accumulation in the dead zone leeway of, or inside the geometry. This demonstrates that, whenever there is a sufficient concentration of phosphate to interact with the solid phase of the porous system, the interaction becomes more dependent on the average pore flow rates.

Higher inlet velocity enhances saturation in cells located favorably in convenient spots (pores opened to outer flow dead zones where ions are gathering), but generally reduces saturation values at most blind cells, as it hinders the accumulation of ions at one position and enables the recovery of phosphate from the porous absorbents (see Fig. 17). Due to this behavior, especially as the temporal influence tends toward negative sensitivity values, the fluid injection rates need to be optimized for effective trapping of phosphate. On the other hand, statistically, applying velocity to a large number of micro-particles may increase crystallization probability at some particles.

As such, due to the diminishing influence of the flow rate over time, optimizing the fluid injection rate is essential for effective crystallization in porous micro-particles. On the other side, increasing the flow rate (velocity) may enhance the likelihood of crystallization in certain micro-particles.

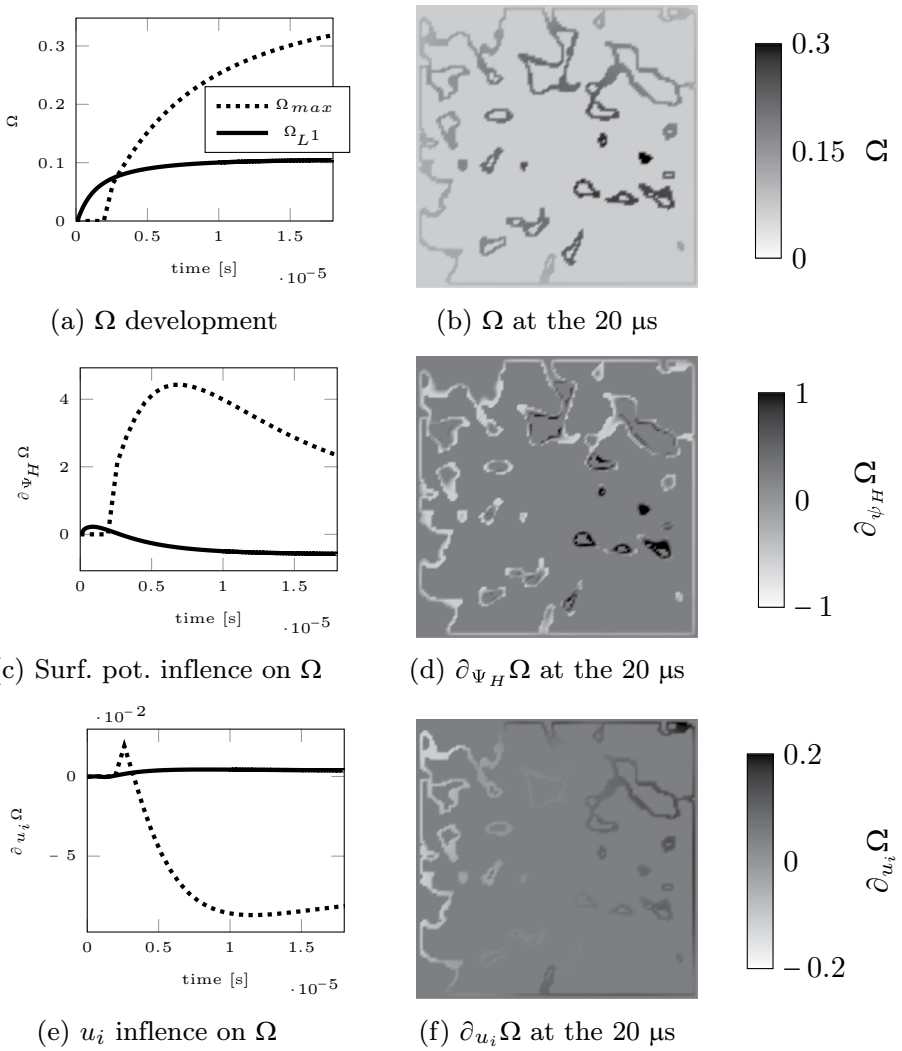

(a) Ω development (b) Ω at the 20 µs

(c) Surf. pot. inflence on Ω (d) $\partial_{\Psi_H}\Omega$ at the 20 µs

(e) u_i inflence on Ω (f) $\partial_{u_i}\Omega$ at the 20 µs

Fig. 15 Temporal development of average and maximal saturation product and its sensitivities (left) and spatial distribution of these values in a middle cut plane. Part I/II

4.3 Influence of hydrogen and phosphate ions concentration

These sensitivity trends (Fig. 16a, b, d, e) are generally weak but consistently positive across all regions. Increasing ion concentrations, as anticipated, results in higher saturation—in particular, in blind pores. The derivative with respect to phosphate concentration is stronger than that with respect to hydrogen concentration. The disparity between average and maximal values of these sensitivities is also substantial.

4.4 Influence of the total porous geometry volume

Considering the anisotropy of the pore structure taken in consideration, it is crucial to investigate the influence of the total pore geometry volume. In the original setup, a quarter of the Estaillades carbonate scan was simulated. Here, 45% of the scan's volume is simulated under identical conditions. The comparison of these two geometries and their resulting saturation products is illustrated in Fig. 18. Simulating a larger portion of the porous rock CT scan results in higher local and average saturation product values that do not stabilize within the simulated time.

As such, we can conclude that a larger geometry accumulates more ions due to longer pores, whilst maintaining the same pore size distribution.

4.5 Verification of 3D sensitivities by setup parameter variation

To verify the sensitivity analysis results of the realistic porous geometry, we consider three different setups (Table 3).

The ions accumulate deeper in the pores when the surface electric potential is increased from Setup I to Setup II. This results in a lower average saturation product, but at the same time, in an increase of the maximum saturation product within the blind pores. Enlarging the geometry increases the average saturation due to the prcence of deeper pores, which in turn, require more time for diffusion processes to

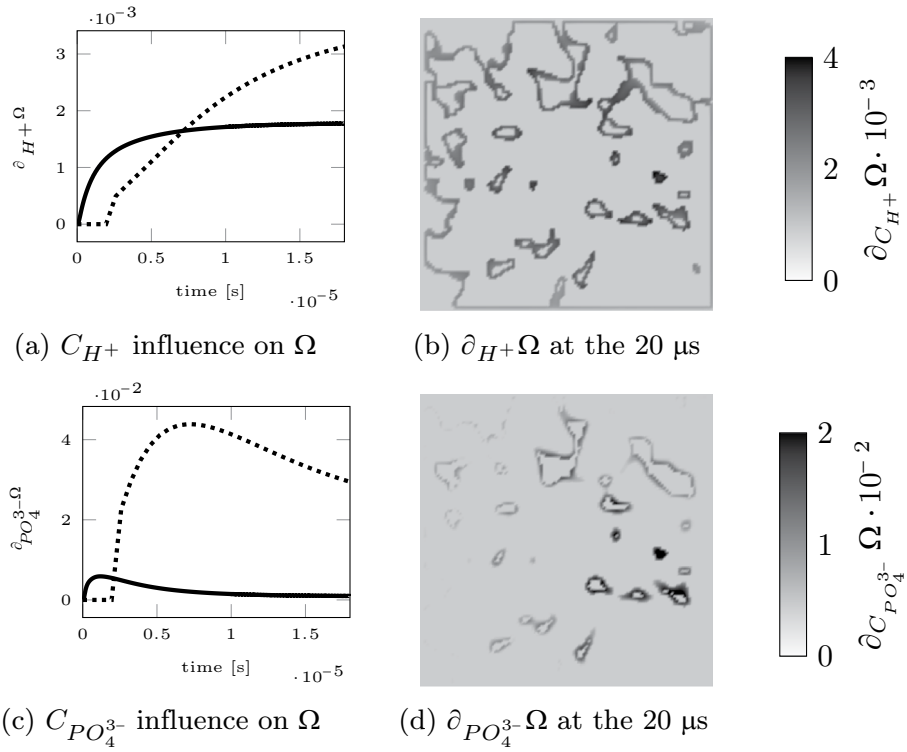

(a) C_{H^+} influence on Ω (b) $\partial_{H^+}\Omega$ at the 20 µs

(c) $C_{PO_4^{3-}}$ influence on Ω (d) $\partial_{PO_4^{3-}}\Omega$ at the 20 µs

Fig. 16 Temporal development of average and maximal saturation product and its sensitivities (left) and spatial distribution of these values in a middle cut plane

(a) With 0.2 $\mathrm{m\,s^{-1}}$ inlet velocity. $\Omega_{max} = 0.455$ (b) Without inlet velocity. $\Omega_{max} = 0.437$

Fig. 17 Saturation product with and without inlet velocity. Visualized are inner cells with $\Omega \geq 0.2$

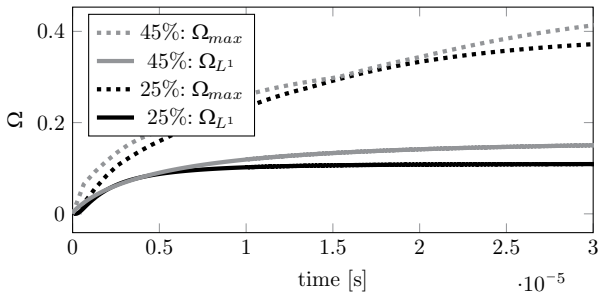

(a) Temporal development of average and maximal saturation products by two geometry sizes

(b) α = 25% (c) α = 45%

Fig. 18 Influence of the porous geometry size on the saturation product development

Table 3 Parameter optimization on a realistic geometry

Setup	I	II	III
ψ_H [V]	+0.01	+0.02	+0.02
$C(H^+)$ [$(\mathrm{mol\,m^{-3}}$]	6	6	6
$C(PO_4^{3-})$ [$(\mathrm{mol\,m^{-3}}$]	1	1	1
u_i [$\mathrm{ms^{-1}}$]	0	0	0
α_{geom} [%]	45	45	100

plateau. This trend is observed in the temporal development of the maximum saturation product in Setup III. In terms of spatial distribution, the saturation product and calcium ion concentration, which has the strongest influence on saturation, primarily accumulate towards the center of the geometry.

For phosphate saturation in CSH particles, the particle size is typically several hundred micrometers. In our current research, we simulated a realistically porous particle with a side length of 0.72 µm. It can be assumed that simulating larger domains will yield higher saturation product values. Investigating this aspect will be part of our future research.

It is observed that increasing the surface potential results in a lower average saturation product, while the maximum

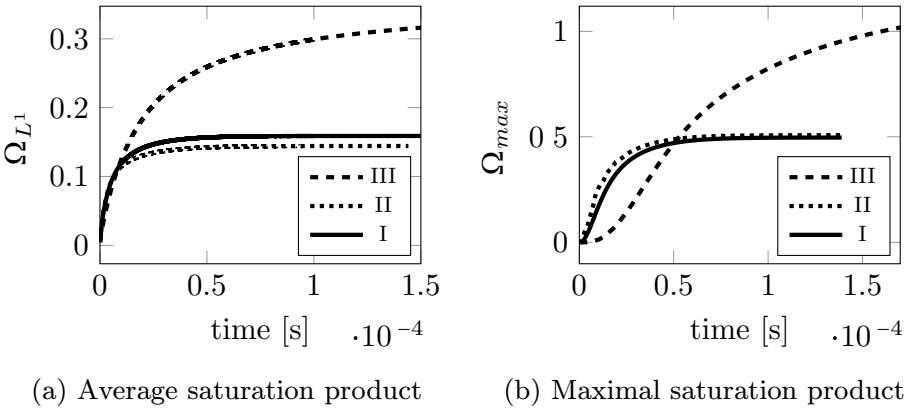

(a) Average saturation product (b) Maximal saturation product

Fig. 19 Saturation products temporal development by Setups I, II and III on a realistic geometry

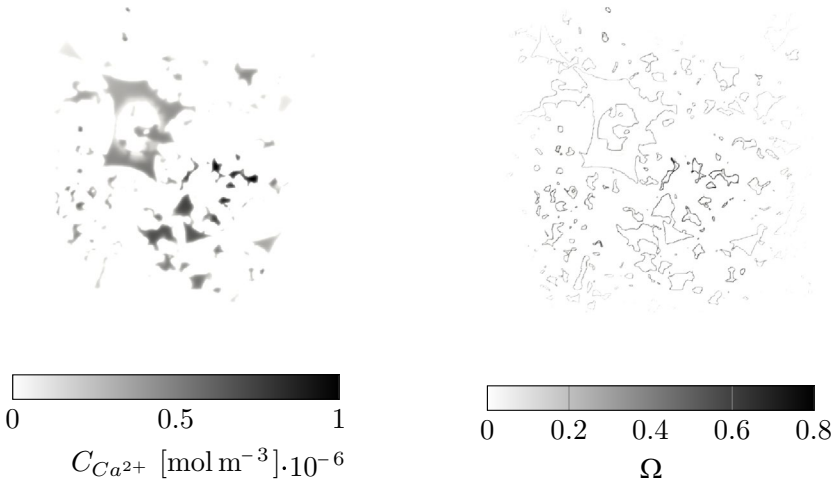

Fig. 20 Distribution of calcium cation concentration and saturation product in the realistic 3D geometry by Setup III at the 170 μs in the middle cut plane

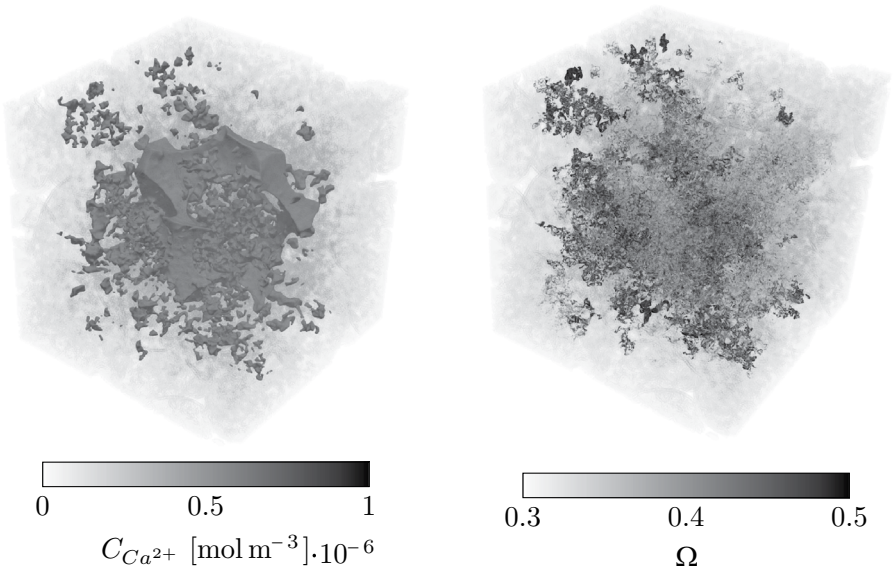

Fig. 21 Spatial distribution of calcium cation concentration and saturation product in the realistic 3D geometry by Setup III at the 170 μs

value of Ω is slightly higher and is reached in a shorter time. This is due to stronger driving electric force based on the potential gradient. The size of the geometry taken in consideration produces the highest influence on the considered values, which grow twice by the Setup III in comparison to the Setup II (Fig. 19). As already investigated in the Sect. 3.3, the highest saturation product is reached in the cells with the highest values of calcium ion concentration, as in the 3D simulations (Figs. 20, 21).

5 Conclusion

The aim of the current research was to explore the dependencies of phosphate saturation in porous CSH particles. Two-dimensional parameterized simplified porous microsystems representing open and blind pores were investigated using a validated RNSPNPE model (cf. Part I), discretized with LBM and combined with forward AD sensitivities computation. A μCT-scan of Estaillades carbonate was taken and scaled to the necessary size for a 3D simulation of phosphate saturation in a realistic porous geometry.

The analysis revealed several key findings:

1. Saturation inside the porous body is significantly higher than on the outer surfaces. In blind pore systems, saturation increases towards the dead end as well as by open pores it grows towards the geometry center shifted along the carrier fluid movement direction.
2. Narrow pore width and large pore length promote oversaturation of the ionic solution, whereby deeper pores extend diffusion times for ions from the bulk.
3. Increasing electric surface potential enhances saturation at the end of blind pores but decreases it in open pores.
4. Higher concentrations of hydrogen and phosphate anions, combined with positive Helmholtz potential, consistently lead to higher saturation.
5. Calcium concentration has the strongest impact on OCP saturation, it can be investigated by observation of the total ion velocity that consists of the carrier fluid velocity, electric and diffusion velocities.
6. Carrier fluid velocity negatively influences saturation in open pores above a certain threshold, but can increase saturation in some blind pores if their inlets are located in dead zones of the flow. However, it decreases saturation in other blind pores. By realistic porous systems it is impossible to predict which velocity direction and which velocity norm size at which pores will increase saturation.
7. Across all pore types, carrier fluid velocity accelerates the filling of pore volumes with ions from the bulk solution.
8. By using a larger geometry, the total pore length is increased, leading to a higher resulting average and local saturation products.

These findings underscore the complex interplay between geometry, surface potential, ion concentrations, and carrier fluid dynamics in determining phosphate saturation within porous CSH systems.

By extending current model with crystallization reaction and adding a new boundary condition which allows fluid cells to become solid according to the formed crystal volume, the full crystallization process can be investigated. This will be part of future work.

Acknowledgements This work was performed on the HoreKa supercomputer funded by the Ministry of Science, Research and the Arts Baden-Württemberg and by the Federal Ministry of Education and Research. The current research is a part of the DFG project number 436212129 "Increase of efficiency in phosphate recovery by understanding the interaction of flow and loading processes with modeling and simulation".

Author contributions F. Bukreev: Methodology, Validation, Formal analysis, Investigation, Software, Data Curation, Writing - Original Draft; A. Kummerländer: Software, Methodology, Writing - Review & Editing; J. Jeßberger: Methodology, Software, Validation, Writing - Review & Editing; D. Teutscher: Writing - Review & Editing; S. Ito: Methodology, Writing - Review & Editing; S. Simonis: Formal analysis, Data Curation, Writing - Review & Editing; Davide Dapelo: Writing - Review & Editing; Mohaddeseh M. Nezhad: Writing - Review & Editing; H. Nirschl: Resources, Funding acquisition; M.J. Krause: Software, Resources, Funding acquisition, Writing - Review & Editing.

Funding Open Access funding enabled and organized by Projekt DEAL.

Data availability No datasets were generated or analysed during the current study.

Declarations

Conflict of interest The authors declare no Conflict of interest.

Declaration of generative AI and AI-assisted technologies in the writing process During the preparation of this work the authors used ChatGPT (OpenAI) in order to improve language. After using this tool, the authors reviewed and edited the content as needed and take full responsibility for the content of the publication.

References

1. Berg U, Knoll G, Kaschka E, Kreutzer V, Weidler PG, Nüesch R (2007) P-roc - phosphorus recovery from wastewater by crystallisation of calcium phosphate compounds. J Res Sci Technol 4(3):117–122
2. Montag D, Everding W, Malms S, Pinnekamp J, Reinhardt J, Fehrenbach H, et al (2015) Bewertung konkreter Maßnahmen einer weitergehenden Phosphorrückgewinnung aus relevanten Stoffströmen sowie zum effizienten Phosphoreinsatz. Umweltbundesamt
3. Egle L, Rechberger H, Zessner M (2014) Endbericht Phosphorrückgewinnung aus dem Abwasser. Technische Universität Wien
4. Ehbrecht A, Fuderer T, Schönauer S, Schuhmann R (2013) Verfahren zur p-rückgewinnung aus abwasser mittels kristallisation: bilanzierung der phosphorströme. KA - Korrespondenz Abwasser Abfall 60(12):1061–1066
5. Ehbrecht A, Schuhmann R (2015) Anwendungsreife erreicht. Das P-RoC-Verfahren ermöglicht die Phosphorrückgewinnung aus Abwässern von Kommunen, Landwirtschaft und Industrie. Verfahren zur P-Rückgewinnung aus Abwasser mittels Kristallisation. ReSource. 28(2):37–45
6. Worch E (2021) Adsorption technology in water treatment: fundamentals, processes, and modeling, 2nd edn. De Gruyter, Berlin
7. Bukreev F, Raichle F, Nirschl H, Krause MJ (2023) Simulation of adsorption processes on moving particles based on an Euler–Euler description using a lattice Boltzmann discretization. Chem Eng Sci 270:118485. https://doi.org/10.1016/j.ces.2023.118485
8. Guan W, Ji F, Chen Q, Yan P, Pei L (2013) Synthesis and enhanced phosphate recovery property of porous calcium silicate hydrate using polyethyleneglycol as pore-generation agent. Materials 6(7):2846–2861. https://doi.org/10.3390/ma6072846
9. Trapote-Barreira A, Cama J, Soler JM (2014) Dissolution kinetics of C–S–H gel: flow-through experiments. Physics and Chemistry of the Earth, Parts A/B/C. 70-71:17–31. Mechanisms and Modelling of Waste-Cement and Cement-Host Rock Interactions. https://doi.org/10.1016/j.pce.2013.11.003
10. Su H, Hu J, Li H (2018) Multi-scale performance simulation and effect analysis for hydraulic concrete submitted to leaching and frost. Eng Comput 34:821–842. https://doi.org/10.1007/s00366-018-0575-9
11. Fukushi K, Okuyama A, Takeda N, Kosugi S (2021) Parameterization of adsorption onto minerals by extended triple layer model. Appl Geochem 134:105087. https://doi.org/10.1016/j.apgeochem.2021.105087
12. Uwaha M (2015) 8—Growth kinetics: Basics of crystal growth mechanisms. In: Nishinaga T, editor. Handbook of Crystal Growth (Second Edition). second edition ed. Boston: Elsevier; pp 359–399. Available from: https://www.sciencedirect.com/science/article/pii/B9780444563699000083
13. Kim D, Mahabadi N, Jang J, van Paassen LA (2020) Assessing the kinetics and pore-scale characteristics of biological calcium carbonate precipitation in porous media using a microfluidic chip experiment. Water Resources Research. 56(2):e2019WR025420. E2019WR025420 2019WR025420. https://doi.org/10.1029/2019WR025420. https://arxiv.org/abs/https://agupubs.onlinelibrary.wiley.com/doi/pdf/10.1029/2019WR025420
14. Ahkami M, Parmigiani A, Di Palma P, Saar M, Kong X (2020) A lattice-boltzmann study of permeability-porosity relationships and mineral precipitation patterns in fractured porous media. Comput Geosci 10:24. https://doi.org/10.1007/s10596-019-09926-4
15. Krause MJ, Kummerländer A, Avis SJ, Kusumaatmaja H, Dapelo D, Klemens F et al (2021) Openlb—open source lattice Boltzmann code. Comput Math Appl 81:258–288. https://doi.org/10.1016/J.CAMWA.2020.04.033
16. Kummerländer A, Bukreev F, Berg S, Dorn M, Krause MJ (2024) Advances in Computational Process Engineering using Lattice Boltzmann Methods on High Performance Computers. In: High performance computing in science and engineering '22. Springer
17. Rouquerol J, Avnir D, Fairbridge CW, Everett DH, Haynes JM, Pernicone N et al (1994) Recommendations for the characterization of porous solids (technical report). Pure Appl Chem 66(8):1739–1758. https://doi.org/10.1351/pac199466081739
18. Chen FF (2016) Diffusion and resistivity. Springer, Cham, pp 145–185
19. Li Z, Li J, Yan G, Galindo-Torres S, Scheuermann A, Li L (2021) Mesoscopic model framework for liquid slip in a confined parallel-plate flow channel. Phys Rev Fluids 6:034203. https://doi.org/10.1103/PhysRevFluids.6.034203
20. Tian F, Li B, Kwok DY (2004) Lattice Boltzmann simulation of electroosmotic flows in micro- and nanochannels. In: 2004 International conference on MEMS, NANO and smart systems (ICMENS'04); pp 294–299
21. Marcus Y (1997) Ion properties / Yizhak Marcus. Marcel Dekker, New York
22. Tung M, Eidelman N, Sieck B, Brown WE (1988) Octacalcium phosphate solubility product from 4 to 37-degree-c. J Res Natl Bur Stand 09(93):613. https://doi.org/10.6028/jres.093.153
23. Heughebaert J, Nancollas G (1984) Cheminform abstract: kinetics of crystallization of octacalcium phosphate. Chemischer Informationsdienst 09:15. https://doi.org/10.1002/chin.198438004
24. Marcus Y (1988) Ionic radii in aqueous solutions. Chem Rev 88(8):1475–1498. https://doi.org/10.1021/cr00090a003
25. DyMAS (2017) A direct multi-scale pore-level simulation approach. vol. Day 3 Tue, April 25, (2017) Of spe western regional meeting; Available from. https://doi.org/10.2118/185720-MS